Phyllotaxis, Pushed Pattern-Forming Fronts, and Optimal Packing

Matthew Pennybacker[*] and Alan C. Newell

Department of Mathematics, University of Arizona, Tucson, Arizona 85721, USA
(Received 12 December 2012; published 13 June 2013)

We demonstrate that the pattern forming partial differential equation derived from the auxin distribution model proposed by Meyerowitz, Traas, and others gives rise to all spiral phyllotaxis properties observed on plants. We show how the advancing pushed pattern front chooses spiral families enumerated by Fibonacci sequences with all attendant self-similar properties, a new amplitude invariant curve, and connect the results with the optimal packing based algorithms previously used to explain phyllotaxis. Our results allow us to make experimentally testable predictions.

Introduction.—The arrangement of phylla (flowers, seeds, stickers, bracts, …) on plants and their surface morphologies have intrigued and mystified scientists from the time of Kepler. A special challenge has been to understand Fibonacci spiral phyllotaxis in which, on many plants, phylla lie on families of visible clockwise and anticlockwise spirals. Counting spirals in each family, called parastichies, results in numbers that follow a Fibonacci progression. Many explanations (Van Iterson [1], Levitov [2] Douady and Couder [3], Atela, Golé, and Hotton [4]) have been teleological in nature and result in discrete models based upon the rules of Hofmeister [5] and Snow and Snow [6] which reflect optimal packing strategies. Mechanistic explanations, the "hows" rather than the "whys," are given in the works of Green, by Meyerowitz, Traas, Kuhlemeier, and Reinhardt, and by Newell, Shipman and colleagues. They have focused on pattern forming physical and biochemical mechanisms: the buckling of the plant's tunica [7], the triggering of auxin inhomogeneities by PIN1 protein transport in cells [8] near its shoot apical meristem (SAM) or combinations thereof [9].

In this Letter, we report on recent numerical results which lend credence to the latter view that almost all features of phyllotactic configurations are the result of a pattern forming front whose origin is a combination of instabilities described above. What is even more surprising but nevertheless gratifying is that the locations of the maxima of the auxin field, which can act as phyllum initiation sites, coincide with the point configurations generated by the discrete models of the teleological approach. This suggests that pattern forming systems may provide a new tool for addressing optimal packing challenges. In short, instability generated patterns may be the mechanism by which plants and other organisms can pursue optimal strategies.

The model we use derives from a continuum approximation to the cell dynamics described in [8]. It assumes that the main contribution comes from the instability of a uniform auxin concentration due to reverse diffusion. This occurs when PIN1 proteins move from the cell interior to the cell wall, where they orient to drive auxin with, and not against, its concentration gradient. The model also makes the simplifying assumption that the surface deformation is slaved to the auxin concentration field via the stress-strain relation, which relates stress to the difference of the total and auxin (growth) induced strains. The resulting partial differential equation is, for certain coefficient choices, a gradient flow given by

$$\frac{\partial u}{\partial t} = -\frac{\delta \mathcal{E}}{\delta u} = \mu u - (\nabla^2 + 1)^2 u - \frac{\beta}{3}(|\nabla u|^2 + 2u\nabla^2 u) - u^3,$$ (1)

$$\mathcal{E}[u] = -\int \frac{\mu}{2}u^2 - \frac{1}{2}(u + \nabla^2 u)^2 + \frac{\beta}{3}u|\nabla u|^2 - \frac{1}{4}u^4,$$ (2)

where u is the fluctuation in auxin concentration about its mean value, t is time, and the system has been scaled so that the most linearly unstable wavelength is 2π. The parameter μ captures the amount by which reverse diffusion driven by PIN1 transport overcomes ordinary diffusion and other loss effects. The parameter β measures how auxin concentration depends on PIN1 distribution.

We study solutions of Eq. (1) in geometries defined by surfaces of revolution. In this Letter we focus on a planar disc geometry, as is the case on a sunflower head. Sunflowers are formed in two stages. In the first, flowers are initiated in an annulus surrounding the SAM and, as the plant grows, the radius of this annulus increases. As a result, the flower configurations evolve into spiral families. At a certain point, however, the SAM undergoes a phase transition and the region on which the seeds form begins to decrease in radius. During this process, the seeds are laid down annulus-by-annulus along an annular front of decreasing radius, and furthermore, each annular pattern remains at the radius at which it was formed. Thus any local optimal packing property which the pattern manifests when it is first laid down remains visible.

To simulate this situation, we initiate a spiral pattern with parastichy numbers M, N (the parastichies in the last
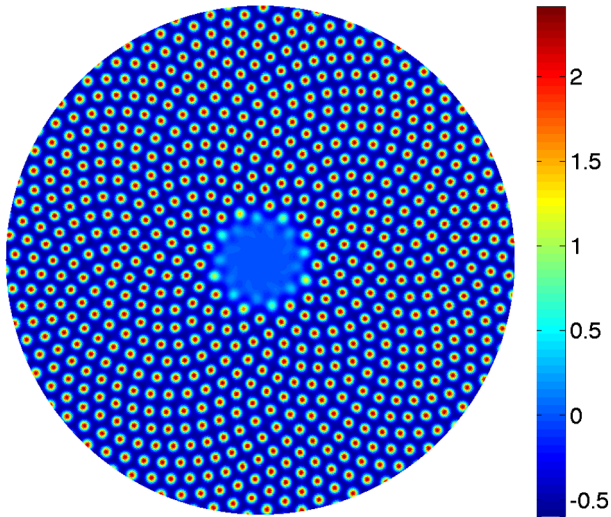
FIG. 1 (color online). A pseudocolor plot of $u(r, \theta)$ on the inner section $r < 89$ of a pattern initiated at $r = 233$ with parastichy numbers $M = 89$ and $N = 144$. A movie [15] may be found in the Supplemental Material.

FIG. 2 (color online). The front speed ν, local energy density ϵ, and local packing efficiency η for $8 < r < 144$. The vertical axis has been rescaled to indicate relative variation from the mean value of each of these quantities.

set of flowers to be laid down in the first phase which sets the outer boundary condition for the seed phase) in an annulus on the outer boundary $r = M + N$ of the disc. The initial conditions are constructed by taking an approximately hexagonal (three-mode) small amplitude solution of Eq. (1) in that region and propagating it on a cylinder of that radius until it reaches a stable nonlinear fixed point. We then use Eq. (1) to propagate this pattern initiated in an annular region of the outer boundary into the interior $r < M + N$ in which the unstable solution $u = 0$ is the initial field.

Results.—In order to classify and understand the pattern that emerges, we decompose the final fixed-time signal $u(r, \theta)$ into circumferential modes and write it in terms of the amplitude and radial phase of each mode as

$$u(r, \theta) = \sum_j a_{m_j}(r) \exp[i(\phi_{m_j}(r) - m_j\theta)] + (\text{c.c.})$$

for all integers m_j. Define the radial wave number by $\ell_{m_j}(r) \equiv -\phi'_{m_j}(r)$. Then, from the sets $\{a_{m_j}(r)\}$ and $\{\ell_{m_j}(r)\}$ we deduce the local structure (in r) of the signal. We find that for any choice of initiating integers M, N, the subsequent final signal has its principal support on that subset of circumferential wave numbers $N, M, N - M, 2M - N, 2N - 3M, \ldots$ generated by the Fibonacci rule. Here we show the results for $M = 89$, $N = 144$ but in [10] display the corresponding results for other pairs including $M = 47$, $N = 76$ which generate the Lucas sequence. The results are also robust for a large open set of choices for μ, β which result in pushed fronts. Here we take $\mu = 0.001$, $\beta = 3$.

Figure 1 is a pseudocolor plot of u on the inner disc $r < 89$ at the time the front has reached $r = 13$. We note
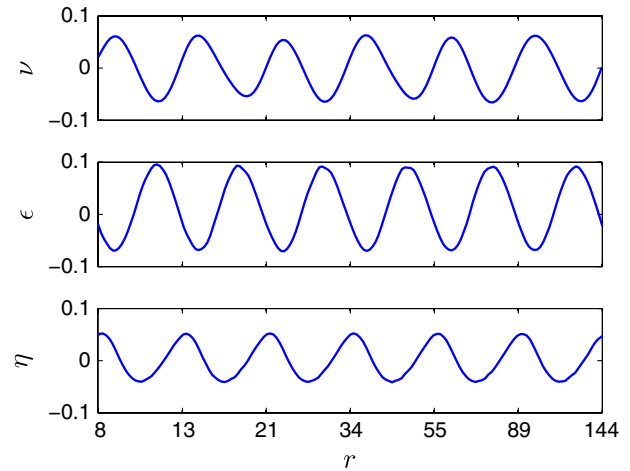
that the visible parastichy numbers decrease with r, and that the transitions between alternating hexagonal and rhombic shapes occur without defects. The radial wave numbers are continuous. Earlier analyses [9], using near-onset amplitude expansions, identified the fixed points corresponding to these shapes but did not prove that the pattern in an annulus at one radius evolves smoothly to that in its neighbor. The partial differential equation simulation does.

Figure 2 shows two measured quantities alongside the front speed ν that is selected by Eq. (1). The local energy density ϵ is the energy (2) in a narrow annulus centered at radius r, scaled by the area of the annulus. The local packing efficiency η is the area fraction of the annulus covered by nonoverlapping equal discs of maximal radius centered at the maxima of the signal. We note that ϵ is minimum at the radii where hexagons dominate and maximum for rhombi. Conversely, for both η and ν the situation is reversed, with the former being due to the fact that hexagons result in better packing than rhombi. The graphs of ν and η are testable predictions, as the front in a developing sunflower head can be experimentally followed [11].

Figure 3 reveals that the evolved pattern is dominated by modes whose circumferential wave numbers belong to the set $\mathcal{F} = \{1, 2, 3, 5, 8, 13, 21, 34, \ldots\}$ defined by the Fibonacci rule $m_{j+1} = m_j + m_{j-1}$. The only other nonzero amplitudes, which have much smaller values, are those corresponding to second harmonics and those generated by the "irregular" Fibonacci rule $m_{j+1} = m_j + m_{j-2}$.

Figure 4 shows that the amplitudes $\{a_{m_j}\}$ for $\{m_j\} = \mathcal{F}$ lie on an invariant curve which exactly captures the self-similar property $a_{m_{j+1}}(r\varphi) = a_{m_j}(r)$, where $\varphi = (1 + \sqrt{5})/2$ is the golden number. Note that in any annulus, there are only three or at most four (two dominant, two
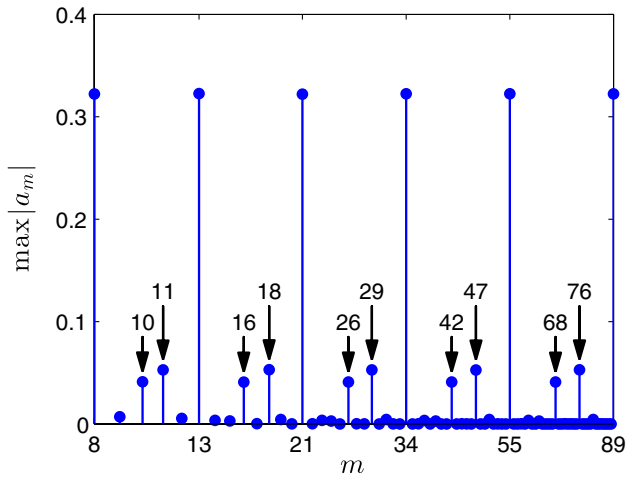
FIG. 3 (color online). The maximum values of the amplitude for all circumferential wave numbers $8 \le m \le 89$.

subdominant) modes present corresponding to the observed hexagonal and rhombic states, respectively. As r decreases, the amplitudes of each mode slide continuously along this curve. This result is completely new and has no analogue in discrete models of phyllotaxis. For example, suppose that points B, C, and D correspond to amplitudes a_{21}, a_{13}, and a_8, respectively. Scaling the radius by φ would yield the same configuration except with B, C, and D corresponding to a_{13}, a_8, and a_5. We also confirm that the radial wave numbers $\{\ell_{m_j}\}$ for $\{m_j\} = \mathcal{F}$ obey the self-similar property $\ell_{m_{j+1}}(r\varphi) = -\ell_{m_j}(r)$. The invariant curve is sharp down to values as low as $r = 8$ with parastichies 3, 5 or down to that radius where the circular eigenfunctions of the Laplacian can be well approximated by $\exp[-i \int \ell_{m_j}(r)dr - im_j\theta]$ in the limit r large, m_j/r finite. For other choices of starting integers M, N on the

outer boundary, the invariant curve has the same shape but is shifted by a calculable amount.

Values of $\{m_j\}$ and $\{\ell_{m_j}\}$ can be used to determine the positions of the maxima, since they occur where the phase $\phi_{m_j}(r) - m_j\theta$ is an integer multiple of 2π simultaneously for all active modes [10]. Because $\ell_{m_j}(r)$ changes slowly compared to the distance between maxima, we may calculate from the radial wave numbers of those modes dominant at a particular r the local radial ρ and angular δ distances between maxima that are laid down consecutively. In botanical terms, these are called the plastochrone difference and divergence angle, respectively.

We are now able to connect our results directly to the point configurations generated by discrete models of phyllotaxis [3,4]. The lattices which are the fixed points of the discrete dynamical systems describing these "locally optimal" point configurations have values of (δ, ρ) which lie on, or near, a branching curve first described by Van Iterson. We overlay our results on the Van Iterson diagram in Fig. 5, where we observe a remarkable coincidence. The maxima of the pattern formed by a pushed front governed by Eq. (1) coincide almost exactly with those point configurations of the discrete approach.

Discussion.—To conclude, we address four questions and pose several open challenges. First, can we understand why, starting from a pattern characterized by integers M, N in the neighborhood of the outer boundary $r = M + N$, only those modes having circumferential wave numbers $N, M, N - M, 2M - N, 2N - 3M, \ldots$ generated by the Fibonacci rule dominate the signal? The evidence provided by the data yields the key clue. Patterns in gradient flows choose configurations with energetically preferred length scales. In Fig. 6, we draw the paths followed by all wave vectors as r decreases to $r = 8$. Only those circumferential
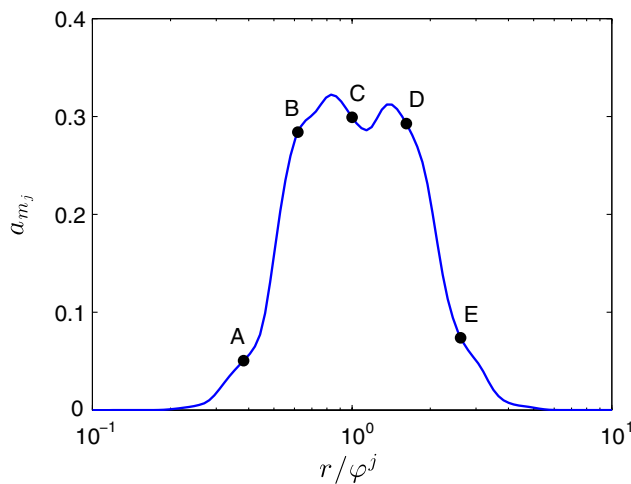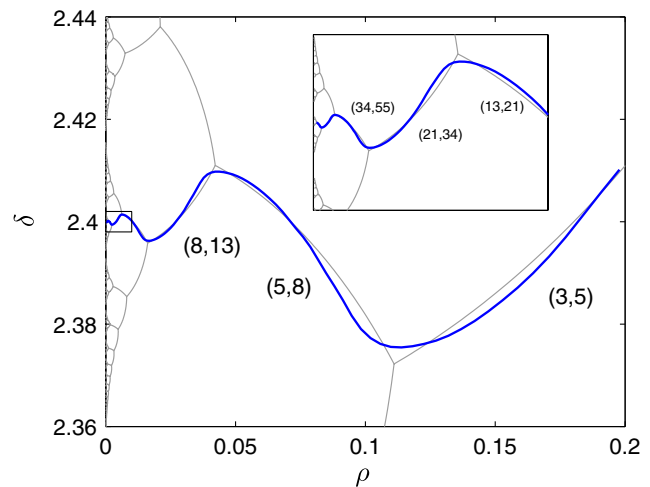

FIG. 4 (color online). The invariant amplitude curve for amplitudes $\{a_{m_j}\}$ with $\{m_j\} = \mathcal{F}$. A movie may be found in the Supplemental Material [16].

FIG. 5 (color online). The values of ρ and δ given by the local approximation at each radius. The shaded lines are the Van Iterson diagram, with selected parastichy numbers indicated. Inset is detail of the data for small ρ.
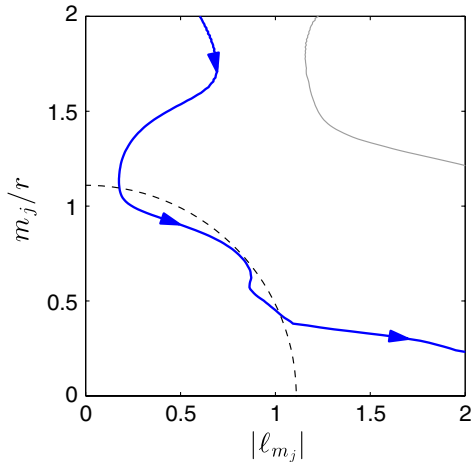
FIG. 6 (color online).   The locus of wave vectors for active Fibonacci modes, with arrows indicating the direction of motion as r decreases. The locus of wave vectors for irregular Fibonacci modes is shaded in the upper right. The dashed semicircle indicates the energetically preferred wave number.

wave numbers generated by the Fibonacci rule approach the energetically preferred wave number k_0, here 1.11, close to, but a nonlinear modification of, the linearly preferred value of unity. The fact that the Fibonacci modes trace the same path reflects the self-similar property mentioned earlier. Moreover, as the pattern moves inward, the next dominant mode in the sequence is principally generated by quadratic interactions reflecting the sign reversal broken symmetry. Effectively this means the corresponding wave vectors add pairwise. As r decreases, the successively generated modes $\mathbf{k}_{N-M}$, $\mathbf{k}_{2M-N}$, $\mathbf{k}_{2N-3M}$, ... move toward the preferred wave number k_0. Their corresponding amplitudes, the pattern order parameters, are therefore dominant.

Second, why do Fibonacci patterns consist of a combination of hexagons and rhombi? In planar geometries, hexagonal configurations dominate because at every location, the quadratic interaction of two modes $\exp(i\mathbf{k}_j \cdot \vec{x})$, $j = 1, 2, |\mathbf{k}_j| = k_0$, 120° apart in angle, generates a mode with wave vector $\mathbf{k}_1 + \mathbf{k}_2$ which also lies on $|\mathbf{k}| = k_0$. Plant patterns do their best to be hexagonal. But because they are laid down, annulus by annulus, by inwardly or outwardly moving fronts, the hexagonal pattern will only fit the circumference at certain radii. In between, only two wave vectors can be close to $|\mathbf{k}| = k_0$ and this gives rise to rhombic structures. In the Supplemental Material, the movie [12] shows the evolution of the wave vectors $\mathbf{k}_5, \mathbf{k}_8, \mathbf{k}_{13}, \mathbf{k}_{21}, \ldots$ alternating between hexagonal and rhombic structures.

Third, why pushed fronts? They are important because the front characteristics are dictated by the pattern behind the front. Bias from the pattern in the neighboring annulus where the pattern has just been laid down affects the choice of (as it turns out weakly unstable) fixed points

corresponding to rhombi which have strongly attracting stable manifolds and weak repelling ones. They also synchronize the front speed of the several modes (three or two) involved in the pattern at any annulus. If the front were pulled, then each of these modes will propagate at a speed depending principally on its radial wave number. The pattern would lose synchrony.

Fourth, we address the nature of the fixed point which represents the Fibonacci pattern shown in Fig. 1. When the region is large enough, the local geometry looks planar and the system should relax to planar hexagonal patches with defects. Careful long time simulations show that the Fibonacci pattern is long, but not infinitely long-lived. For a case shown in the Supplemental Material [13], as the front evolves along the stable manifold of the Fibonacci pattern, the energy (2) decreases 1890 units in 75 time units. The pattern remains nearly stationary for another 250 time units, after which the energy has only decreased 2 additional units. Then we see a further decrease which is manifested by reorganization of the maxima and eventually the appearance of defects in the rhombic regions which are the least optimally packed. This is consistent with our observations when we evolve the pattern on a cylinder of fixed radius. The spiral hexagonal solutions are stable. The rhombic solutions are susceptible to Eckhaus-like instabilities. Thus, while Fibonacci patterns would seem to be universal in situations where the pattern is laid down annulus by annulus, they are in fact long-lived transients. In plants, however, there may be additional mechanisms so that phylla, once initiated, become rooted and thereafter move with the growing plant.

We end this Letter with several challenges. Will the coincidence of the maxima of a pushed pattern-forming front and that point configuration generated by locally optimal packing algorithms be still valid in three dimensions? Can one associate a corresponding pattern forming system with every optimal packing challenge? It is interesting that a similar connection has been reported in another context [14]. Finally, we ask: How might one be led to anticipate from *a priori* reasoning that the pushed pattern front solutions of Eq. (1) have so many invariants and self-similar properties when there is no obvious simple scaling transformation of the original Eq. (1)?

*pennybacker@math.arizona.edu
[1] I. van Iterson, *Mathematische und Mikroskopisch-Anatomische Studien über Blattstellungen nebst Betrachtungen über den Schalenbau der Miliolinen* (Gustav Fischer, Jena, 1907).
[2] L. S. Levitov, Phys. Rev. Lett. **66,** 224 (1991).
[3] S. Douady and Y. Couder, Phys. Rev. Lett. **68,** 2098 (1992); J. Theor. Biol. **178,** 255 (1996); **178,** 275 (1996); **178,** 295 (1996).

[4] P. Atela, C. Golé, and S. Hotton, J. Nonlinear Sci. **12,** 641 (2003).

[5] W. Hofmeister, *Allgemeine Morphologie der Gewachse*, Handbuch der Physiologischen Botanik (Engelmann, Leipzig, 1868).

[6] M. Snow and R. Snow, Proc. R. Soc. London, Ser. B **139,** 545 (1952).

[7] P. Green, Am. J. Bot. **86,** 1059 (1999).

[8] D. Reinhardt, T. Mandel, and C. Kuhlemeier, Plant Cell **12,** 507 (2000); D. Reinhardt, E.-R. Pesce, P. Stieger, T. Mandel, K. Baltensperger, M. Bennett, J. Traas, J. Friml, and C. Kuhlemeier, Nature (London) **426,** 255 (2003); P. B. de Reuille, I. Bohn-Corseau, K. Ljung, H. Morin, N. Carraro, C. Godin, and J. Traas, Proc. Natl. Acad. Sci. U.S.A. **103,** 1627 (2006); H. Jönnson, M. Heisler, B. Shapiro, E. Meyerowitz, and E. Mjölsness, Proc. Natl. Acad. Sci. U.S.A. **103,** 1633 (2006).

[9] A. C. Newell, P. D. Shipman, and Z. Sun, J. Theor. Biol. **251,** 421 (2008); A. C. Newell and P. D. Shipman, Anal. Appl. **06,** 383 (2008).

[10] A. C. Newell and M. Pennybacker, Procedia IUTAM (to be published).

[11] S. Hotton, V. Johnson, J. Wilbarger, K. Zwieniecki, P. Atela, C. Golé, and J. Dumais, J. Plant Growth Regul. **25,** 313 (2006).

[12] See Supplemental Material at http://link.aps.org/supplemental/10.1103/PhysRevLett.110.248104 for a movie of the wave vector motion as r decreases.

[13] See Supplemental Material at http://link.aps.org/supplemental/10.1103/PhysRevLett.110.248104 for a graph of the dissipation rate $-d\mathcal{E}/dt$ as the pattern evolves on the annulus $55 < r < 89$.

[14] D. K. Lubensky, M. W. Pennington, B. I. Shraiman, and N. E. Baker, Proc. Natl. Acad. Sci. U.S.A. **108,** 11 145 (2011).

[15] See Supplemental Material at http://link.aps.org/supplemental/10.1103/PhysRevLett.110.248104 for a movie of the evolution of Eq. (1) on the disc $r < 89$.

[16] See Supplemental Material at http://link.aps.org/supplemental/10.1103/PhysRevLett.110.248104 for a movie of the amplitudes $\{a_{m_j}(r)\}$ for $\{m_j\} = \mathcal{F}$ moving over the invariant curve.